

# Paper-based laser-pyrolyzed electrofluidics: an electrochemical platform for capillary-driven diagnostic bioassays

Léonard Bezinge, Jake M. Lesinski, Akkapol Suea-Ngam, Daniel A. Richards\*, Andrew J. deMello\* and Chih-Jen Shih\*

*Institute for Chemical and Bioengineering, Department of Chemistry and Applied Biosciences, ETH Zürich, Vladimir-Prelog-Weg 1, 8093 Zürich, Switzerland.*

\* Corresponding authors: D.A.R. ([daniel.richards@chem.ethz.ch](mailto:daniel.richards@chem.ethz.ch)), A.J.D. ([andrew.demello@chem.ethz.ch](mailto:andrew.demello@chem.ethz.ch)) and C.J.S. ([chih-jen.shih@chem.ethz.ch](mailto:chih-jen.shih@chem.ethz.ch))

## Abstract

Microfluidic paper-based analytical devices ( $\mu$ PADs) are indispensable tools for disease diagnostics. The integration of electronic components into  $\mu$ PADs enables new device functionalities and facilitates the development of complex quantitative assays. Unfortunately, current electrode fabrication methods often hinder capillary flow, considerably restricting  $\mu$ PAD design architectures. Here, we present laser-induced graphenization as an approach to fabricate porous electrodes embedded into cellulose paper. The resulting electrodes not only have high conductivity and electrochemical activity, but also retain wetting properties for capillary transport. We demonstrate paper-based electrofluidics, including (i) a lateral flow device for injection analysis of alkaline phosphatase in serum and (ii) a vertical flow device for quantitative detection of HPV16 with a CRISPR-based assay. We expect that this platform will streamline the development of diagnostic devices that combine the operational simplicity of colorimetric lateral flow tests with the added benefits and possibilities offered by electronic signaling.

## Introduction

Microfluidic paper-based analytical devices ( $\mu$ PADs) are an important class of microfluidic devices capable of performing total (bio)chemical analysis at ultralow cost (1). The strength of  $\mu$ PADs lies in their ability to move fluids *via* passive capillary action without the need for external fluid actuation, thus enabling complex bioassays with extraordinary simplicity (2). The integration of electronic components into  $\mu$ PADs has attracted substantial attention for its potential to realize new functionalities and capabilities. Indeed, the incorporation of electrodes opens the door to quantitative electrochemical detection (3), assay miniaturization (4) and advanced connectivity (e.g., via near-field wireless communications) (5, 6). However, electrode fabrication on paper is immensely challenging due to the rough and inhomogeneous nature of cellulose materials. In addition, the cost and complexity of current fabrication techniques hinder single-use applications.

Dungchai *et al.* (7) reported electrochemical detection on paper using screen-printed electrodes. Since then, a wide variety of deposition techniques have been developed and further refined, including inkjet printing (8, 9), screen printing (10–12), metal sputtering (13), thermoplastic forming (14, 15) and pencil drawing (16). Most of these techniques are derived from conventional manufacturing processes for printed electronics. However, these deposited electrodes are often hydrophobic, hinder capillary flow and display limited contact with the fluid within pores.

There have been several attempts to circumvent these limitations. For example, Hamedi *et al.* (17) reported paper-based devices incorporating embedded electrodes and microfluidics through the combination of wax channel patterning and drop-casted conductive inks. They showcased a variety of electronic circuits triggered by capillary flow. Nevertheless, these approaches do not allow independent patterning of flow paths and electronic circuit traces. This means that the electrodes are constrained within the channel boundaries and it is not possible to fabricate multiple electrodes separated with electrolytes on a single sheet. This considerably limits potential applications within electrochemical sensing.

Very recently, researchers have begun to explore the direct conversion of insulating polymers, such as polyimide (Kapton) (18) and a variety of commercial polymers (19), to conductive graphenic materials using CO<sub>2</sub> laser cutters/engravers. In particular, laser-pyrolized polyimide substrates have been used in a number of biosensing applications, including small molecule detection (20, 21), protein-based immunoassays (22, 23), and DNA (24) or miRNA (23) recognition. Laser-induced pyrolysis of cellulose is a comparatively nascent field and to date has been exploited for artistic depictions (25), simple electric circuits (26), mechanical sensing (27, 28), and more recently small molecule detection (29–32). Despite early successes, it remains unclear whether cellulose has any advantage over polyimide as a substrate material for laser-induced graphenic electrodes (LIG-Es), aside from biodegradability.

Inspired by recent progress in laser-induced graphenization, we present a method for patterning electrofluidic paths directly onto cellulose. We show that these patterns can be used to transmit both fluid and electrical currents and can be leveraged to create novel electrochemical biosensing assays. Ultimately, this work demonstrates that cellulose paper is an ideal substrate for LIG-Es, and paves the way towards a range of novel sensing applications.

## Results

The electrochemical paper platform presented here relies on the combination of wicking channels and electronic signal traces. The intertwined patterns of these two components are embedded in a sheet of cellulose paper and together create functional electrofluidic layers. The fabrication process is as follows (Fig. 1a). First, paper-embedded electrodes are generated *via* laser-induced pyrolysis, harnessing the high carbon content of cellulose to create graphenic conductive traces *in situ*. Next, fluidic channels are formed by laminating wax onto the cellulose. It is noteworthy that the patterns for electrodes and channels are fully independent, enabling the fabrication of individually isolated and superimposed regions, with full control over wetting and conductive properties (Fig. 1b). Remarkably, the process is scalable; per A4 sheet of cellulose paper, we can fabricate up to 176 sensors within 90 minutes at a cost of under \$0.02 per sensor at a prototyping scale (Fig. 1b and Table S1).

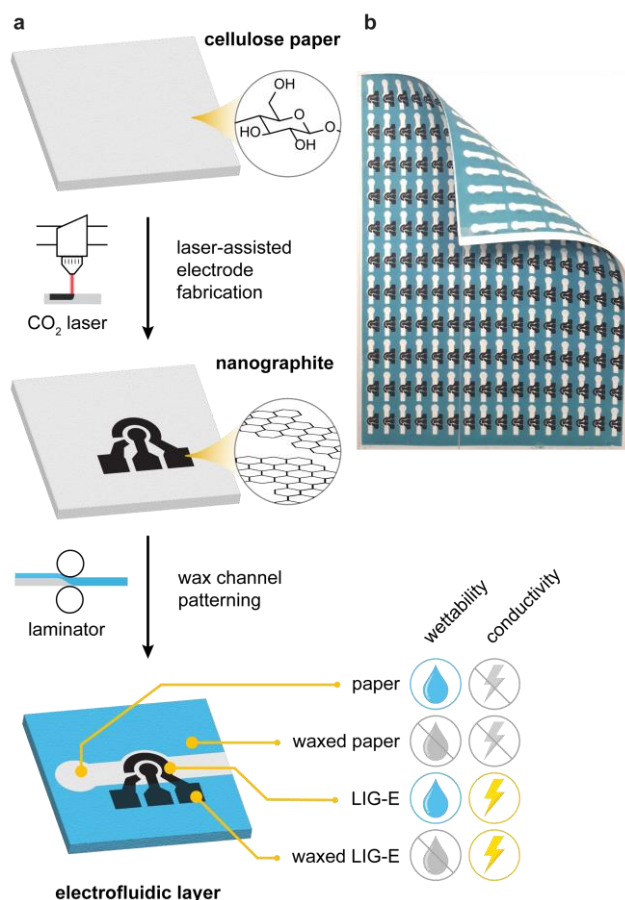


**Fig. 1. Fabrication of paper-based electrofluidic systems.** (a) The paper-embedded electrodes are created by laser-induced pyrolysis of cellulose, followed by the patterning of fluidic channels by wax lamination. This process allows for independent patterning of electrodes and channels, enabling full control over the wetting and conductive properties in different regions. (b) Photograph of an A4 paper sheet containing 176 sets of electrochemical cells embedded in a fluidic channel.

### Understanding the formation of laser-induced graphenic paper

We first set out to elucidate the mechanisms underpinning the laser-induced pyrolysis of cellulose. Despite the rapidly growing interest in laser-induced graphenization, underlying mechanisms remain poorly understood (33). The pyrolysis of polyimide involves the transformation of a homogeneous polymer solid into a foam-like structure due to the rapid generation of gaseous products during the photothermal process (18, 33). The pyrolysis of cellulose is more challenging, since the porous and fragile nature of the substrate, combined with its high oxygen content and lack of aromaticity, reduces

the window of process conditions suitable for successful graphenization. Two key parameters help in this regard: pre-treatment with a fire-retardant solution and laser defocusing (19, 25). The former prevents complete combustion of the cellulose fibers by promoting recombination reactions, and the latter effectively exposes the substrate to multiple laser pulses. To explore this idea, we screened a number of inorganic fire-retardant salts together with different laser parameters. We identified ammonium sulfamate as the best pre-treatment agent, yielding a sheet resistance as low as  $23 \pm 2 \text{ } \Omega \text{ sq}^{-1}$  (Figs. S1 and S2). It should be noted that this value is significantly lower than previously reported sheet resistances (31, 32) and comparable to laser-pyrolyzed polyimide (down to  $15 \text{ } \Omega \text{ sq}^{-1}$ , Table S2) (18)

Next, taking inspiration from furnace-based pyrolysis (34–36), we employed Raman spectroscopy and wide-angle X-ray scattering (WAXS) to investigate the formation of graphenized cellulose (Fig. 2). We examined laser powers between 1.2 and 4.8 W at 10 mm laser defocus and a speed of  $16 \text{ cm s}^{-1}$ . The lower bound approximately corresponds to the power that results in a degree of visible carbonization, and the upper bound corresponds to the maximum power the paper can endure without compromising mechanical integrity (Fig. 2a and S2). At low powers, we observed superficial carbonization of cellulose fibers with no detectable conductivity (Fig. 2b), while increasing the power beyond 2.4 W led to a sudden drop in sheet resistance.

Raman spectroscopic analysis of the pyrolyzed cellulose revealed further details on the formation of graphenic material (Fig. 2c). For superficially-pyrolyzed samples, the fluorescence signal from the cellulose paper dominates, but this disappears as the electrical resistance decreases. In addition, the peaks characterizing the  $\text{sp}^2$ -hybridized carbon network (G band) and the finite lateral size of the graphitic crystallites (D band) (37) emerge at  $1577 \pm 2 \text{ cm}^{-1}$  and  $1339 \pm 2 \text{ cm}^{-1}$ , respectively. By increasing the laser power from 2.4 to 4.8 W, the ratio of D-band to G-band peak areas gradually decreases, indicating lateral growth of crystallite domains (37). Conversely, the 2D band at  $2665 \pm 5 \text{ cm}^{-1}$ , originated from the D-band overtone and sensitive to graphene stacking, (38) becomes more prominent as laser power increases, evidencing the emergence of thin graphene domains. The multi-component and broadband nature of the 2D-overtone (Figs. S3 and S4) further suggests a high degree of graphitization

with turbostratic stacking between the graphenic layers (35). Notably, we did not observe significant shifts in peak positions upon growth of the crystallite domains (Fig. S5).

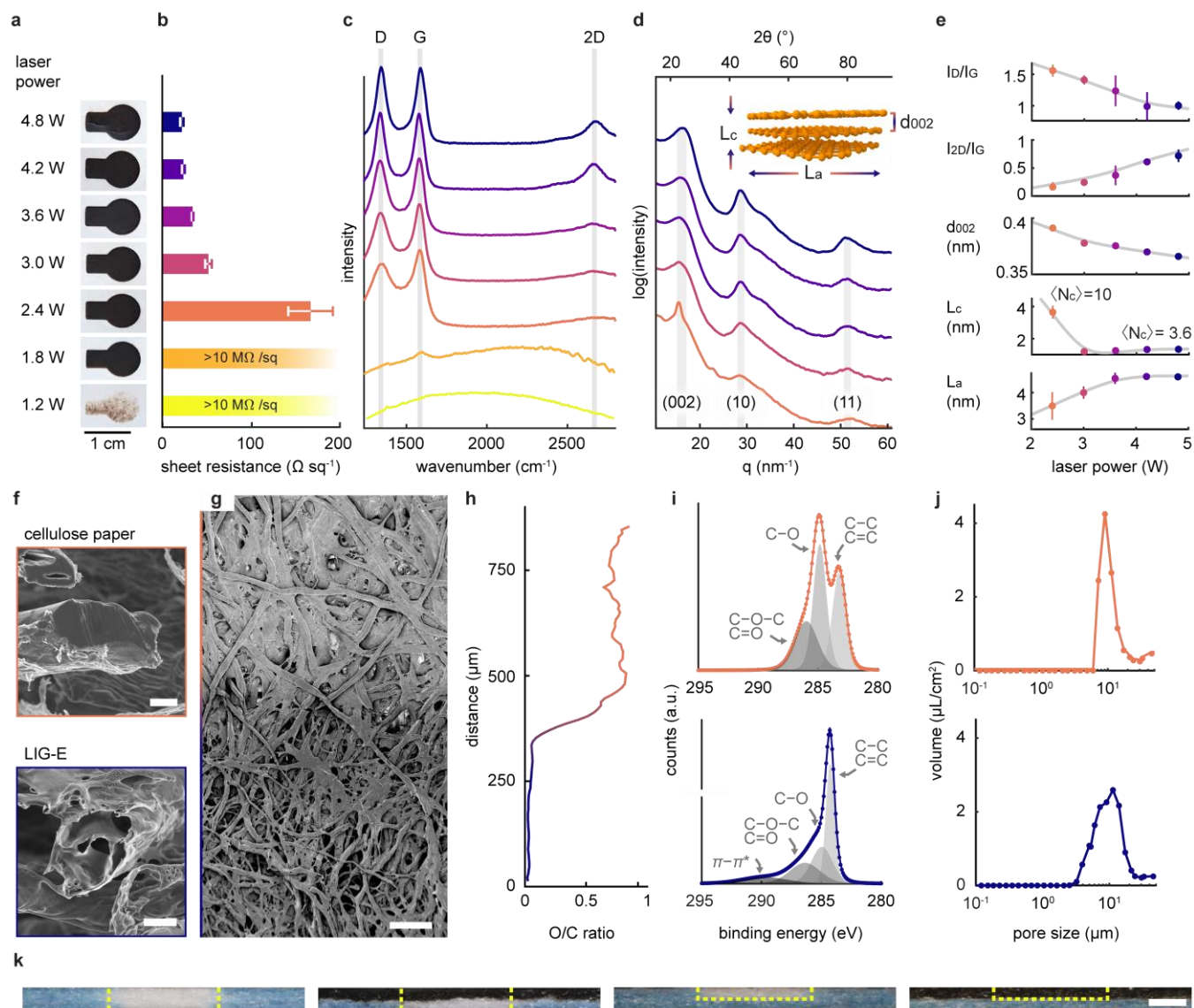


**Fig. 2. Unveiling the formation and structure of laser-pyrolyzed cellulose paper.** (a) Photographs of LIG-Es fabricated using variable laser powers with (b) corresponding sheet resistances. (c) Confocal Raman spectra for the considered samples, showing the emergence of the D, G, and 2D bands that are characteristic of graphenic materials. (d) WAXS diffractograms for the pyrolyzed materials, with the (002), (10) and (11) diffraction peaks highlighted. Inset: schematic of a nanographitic crystallites with lateral size,  $L_a$ , thickness,  $L_c$  and interlayer spacing,  $d_{002}$ . (e) Comparison of spectroscopic parameters extracted from Raman and XRD measurements as a function of laser power. (f) Cross-sectional SEM images for a cellulose fiber before (top; orange) and after (bottom; purple) laser-induced pyrolysis. Scale bars: 5  $\mu\text{m}$ . (g) Top-view SEM image of a cellulose-LIG-E interface revealing the morphological transition. Scale bar: 100  $\mu\text{m}$ . (h) Corresponding oxygen-to-carbon ratio across the interface informed

by EDX. (i) XPS spectra near the C1s region and (j) mesopore size distributions characterized by mercury porosimetry for cellulose (top) and LIG-E (bottom). (k) Cross-sectional photographs for the four different types of fabricated channels. From left to right: flow-through paper, flow-through LIG-E, lateral-flow paper, and lateral-flow LIG-E. The yellow dashed lines define channel boundaries confined with wax barriers. Scale bar: 500  $\mu\text{m}$ .

Early reports on the formation of laser-pyrolyzed conductive materials have relied exclusively on Raman spectroscopy (39). However, this approach provides a qualitative, or at best semi-quantitative, assessment of structural parameters. To gain quantitative insights into the evolution of their structural parameters, we carried out wide-angle X-ray scattering (WAXS) to correlate materials conductivity with graphenic crystallography. After isolating the pyrolyzed material, we were able to identify diffractograms of graphitic materials exhibiting the (002), (10) and (11) diffraction peaks (Figs. 2d and S6). It should be noted that turbostratic layered materials have indistinguishable (101) and (100) peaks, and are thus assigned as (10) here; the same applies to the (11) peak.

We estimated the crystallite size of our pyrolyzed materials using the Scherrer equation (34, 40). This analysis revealed that by increasing the laser power from 2.4 to 4.8 W, the crystallite lateral size,  $L_a$ , extracted from the (10) peak, grows from  $3.5\pm 0.4$  to  $4.6\pm 0.1$  nm. On the other hand, the crystallite thickness  $L_c$ , extracted from the (002) peak, reduces from  $3.8\pm 0.4$  to  $1.32\pm 0.04$  nm, corresponding to  $10\pm 1$  and  $3.6\pm 0.1$  stacking layers of graphene, respectively (Fig 2e). Similar crystallite parameters could be attained in wood samples pyrolyzed in a furnace at between 1000 and 2000  $^{\circ}\text{C}$  (34). Furthermore, upon increasing the laser power, the average interlayer distance informed by the  $d$ -spacing of the (002) peak,  $d_{002}$ , gradually decreases from 0.4 nm to 0.37 nm, approaching that for AB-stacking graphite (0.335 nm), in spite of its turbostratic nature. The graphenic crystallites appear to grow laterally and interconnect, resulting in 7-fold drop in macroscopic electrical resistance. Furthermore, the small crystallite sizes, combined with their reduced thickness (a few layers), offer edge-rich graphene for efficient electrochemical detection (41).

It is worth mentioning that previous studies for laser-pyrolized graphenic materials estimated the crystallite sizes from the Raman D/G peak ratios using a popular model established by Cançado *et al.* (18, 29, 37). Compared to our values informed by WAXS, we found that the Cançado model overestimates the lateral dimension by four times (Fig. S7). This is unsurprising as the semi-empirical model was developed for top-down fabricated, highly-pure nanographite samples, rather than semi-crystalline materials or materials derived from precursors containing heteroatoms.

In practice, the macroscopic structural and surface properties of the pyrolyzed paper heavily influence LIG-E wetting and electrochemical responses in functional devices. To explore these features, we studied LIG-E using electron microscopy, and discovered that the fibrous structure of cellulose is conserved after pyrolysis (Fig. 2f and 2g). As anticipated, analysis of energy-dispersive X-ray (EDX) spectra revealed that pyrolysis successfully removed over 95% of the oxygen atoms from the bulk paper material (Fig. 2h). Interestingly, we did not detect any significant incorporation of nitrogen or sulfur atoms in the carbonaceous structure (Fig. S8).

Advanced chemical analysis by the X-ray photoelectron spectroscopy (XPS) corroborated the EDX results. Despite a significant reduction of oxygen content, we still observed a considerable fraction of C-O and C=O surface functional groups (Fig. 2i). These hydrophilic functional groups are desirable to retain good wettability and could serve as anchor points for surface functionalization. Mercury porosimetry further revealed that the cellulose paper and LIG-E exhibit nearly identical mean pore sizes (11  $\mu\text{m}$ ), with a small degree of distribution broadening (Fig. 2j). The conservation of cellulose wetting and mesoporous properties after laser pyrolysis makes LIG-E extremely promising for applications in capillary-driven electrofluidic systems.

To explore the seamless integration of LIG-E with fluidic channels, we combined laser-induced pyrolysis with double-layer lamination (top and bottom) of pre-patterned wax. Depending on the configuration, capillary flow can either extend through the whole sheet (vertical channels) or confine

within the electrode depth along the surface (lateral channels) (Fig. 2k). Importantly, we found that the conductive properties remain unaffected by the wax channel interfaces (Fig. S9).

### **Engineering anisotropic capillary-flow properties**

Next, we examined and engineered the wicking properties of our channel architectures in various flow configurations, since effective wetting within the porous LIG-E structure is essential to maximizing electrode utilization for sensing applications. The wetting properties of laser-pyrolyzed polyimide can be tuned by control of the lasing atmosphere (42),  $\text{KMnO}_4$  pre-treatment (43), and post-modifications (44). In our cellulose systems, we found that the laser-pyrolyzed electrodes are always superhydrophilic, completely absorbing a water droplet within  $< 50$  ms. This is comparable to unmodified cellulose paper (Fig. 3a) regardless of the lasing atmosphere (Fig. S10). It should be noted that we used “wetting time” to evaluate hydrophilicity since water contact angles cannot be measured on wicking substrates. Importantly, the LIG-E fabricated on paper remained superhydrophilic after more than a week of storage under ambient conditions (Fig. S11). On the other hand, we rendered paper or LIG-E hydrophobic (static water contact angles of  $117\pm 8^\circ$  and  $129\pm 2^\circ$ ) through lamination of a wax pattern (Fig. 3a). This technique opened up the possibility of creating flow channels that are unaffected by the presence of electrodes and isolate the electrode contacts from the fluidic channel (Fig. S12).

Although assessment of static wetting properties offers useful information, we questioned whether the results could be transferred to more intricate flow-based systems. Paper-based devices are generally designed around specific flow configurations, such as lateral flow (with the front moving in-plane along the paper sheet), vertical flow (with the flow perpendicular to the stacked layers), or a combination thereof (three-dimensional paper microfluidic networks). This is an important consideration for the electrofluidic layers fabricated here, as the directional nature of the lasing process yields LIG-E of anisotropic structure, which may interact differently with varying flow directions. To explore this, we flowed water through LIG-E embedded in cellulose and compared the fluid front positions as a function of time for neat paper, LIG-E, and oxygen plasma-treated LIG-E in different flow formats (Fig. S13). In a lateral flow format (Fig. 3b), LIG-E acts as a flow delay compared to neat paper ( $51\pm 4$  s delay for

a 4 mm long electrode, Fig. S14) because its deep structure is hydrophobic (45). Treatment of the LIG-E with oxygen plasma (before the wax patterning step) induces capillary-driven lateral flows similar to that of cellulose paper (Fig. 3c), likely due to the introduction of hydrophilic oxygen-rich moieties on graphenic surfaces (46). On the other hand, in a vertical flow configuration (Fig. 3e), the LIG-E exhibits unobstructed capillary flow irrespective of oxygen plasma treatment (Fig. 3f). This result agrees with the contact angle measurements. We fitted the capillary front profile using the Washburn equation according to  $L = (D_w \cdot t)^{0.5}$  where  $L$  is the front position,  $D_w$  is the Washburn diffusion coefficient and  $t$  is time (47, 48). We found that the LIG-E diffusion coefficient in lateral flow reduces approximately by six-fold compared to untreated paper or plasma-treated LIG-E (Fig. 3d).

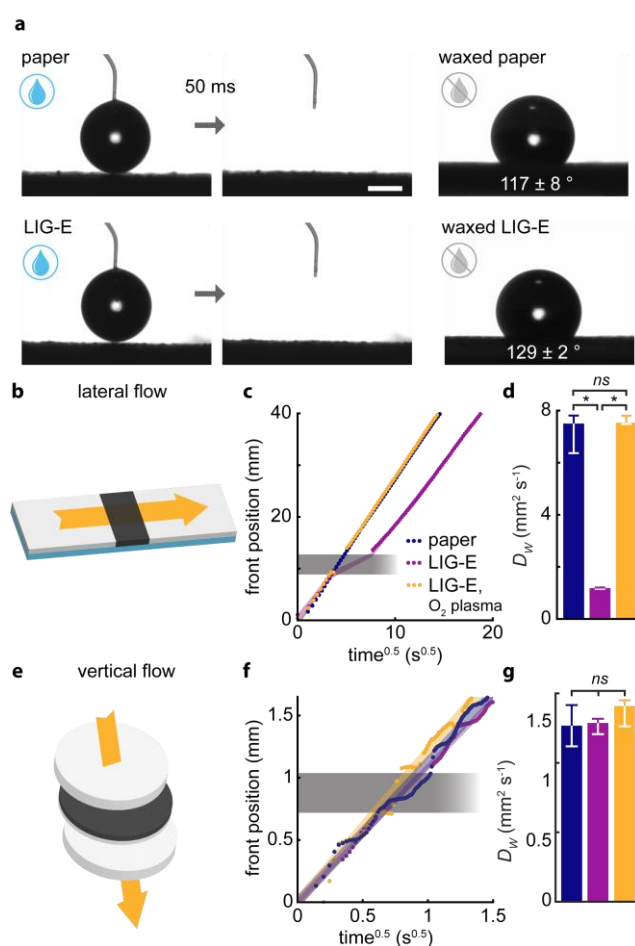


**Fig. 3. LIG-E wicking properties in lateral and vertical capillary flow configurations.** (a) Contact angle measurements for four combinations of wax and LIG-E channels. Neat paper and LIG-E absorb a water droplet within  $< 50\text{ ms}$ , whereas waxed cellulose and LIG-E exhibit static hydrophobicity with

high contact angles. Scale bar: 500  $\mu\text{m}$ . A lateral capillary-driven flow (b) is evaluated by monitoring the waterfront as a function of time (c) across a strip of neat paper, LIG-E, and oxygen plasma-treated LIG-E. The shaded areas correspond to fits to the Washburn equation including standard deviations, which allow us to extract the Washburn diffusion coefficients (d). Similarly, in a vertical flow configuration (e), we characterized the front positions (f) and extracted their Washburn diffusion coefficients (g). The grey zones in panels (c) and (f) represent the duration of flow across the materials.

Interestingly, while wicking through lateral channel networks has been extensively studied (49), the vertical flow dynamics across multilayers structures in an out-of-plane direction have never been explored, despite their applications in many commercial diagnostic devices (50). Surprisingly, we found that vertical flows exhibit Washburn diffusion coefficients approximately 5-fold lower than their lateral counterparts (Fig. 3g), despite significantly shorter timescales and smaller diffusion distances. We hypothesize that the slower wicking observed in vertical configurations is due to the in-plane fiber direction and non-ideal contact between cellulose layers.

### **Linking capillary wetting to electrochemical properties**

In view of the anisotropic flow properties of the LIG-E, we examined its electrochemical characteristics with the aim of correlating these with capillary properties. The permeable electrodes and their unique wicking properties form the building block of the electrochemical platform. For this reason, understanding the effect of wetting on electrochemical performance is essential. We designed and fabricated our electrochemical sensors using a three-electrode configuration, in which voltages are applied and reported relative to a pseudo-reference LIG-E, instead of a standard reference electrode, such as silver/silver chloride. This way, the simplicity and scalability of the fabrication process is greatly improved, while still being sufficiently accurate for almost all electrochemical sensing methodologies.

First, we investigated the effect of LIG-E wettability on the effective electroactive areas using a standard redox probe (ferro-/ferricyanide) in two different flow configurations (Fig. 4a). We interrogated the electrodes using cycling voltammetry (Fig. 4b) and computed the electroactive area using the Randles-Ševčík equation for diffusion-controlled processes (Fig. 4c) (51). The electrochemical porosity factor,  $\eta$ , is defined as the ratio of the electroactive area to the projected area (from the design). In lateral flow,

we found that  $\eta = 1 \pm 0.4$  for LIG-E due to poor wettability, but is drastically increased ( $\eta =$  up to 4.0) in oxygen plasma-treated LIG-E (Fig. 4d). On the other hand, and echoing the moving front experiment, we observed high porosity factors in the vertical flow format for both LIG-E and plasma-treated LIG-E, showing  $\eta = 5.7 \pm 0.2$  and  $6.3 \pm 0.3$ , respectively. These findings suggest that the top surface is both hydrophilic and electroactive, although it is not fully accessible in lateral flow configurations.

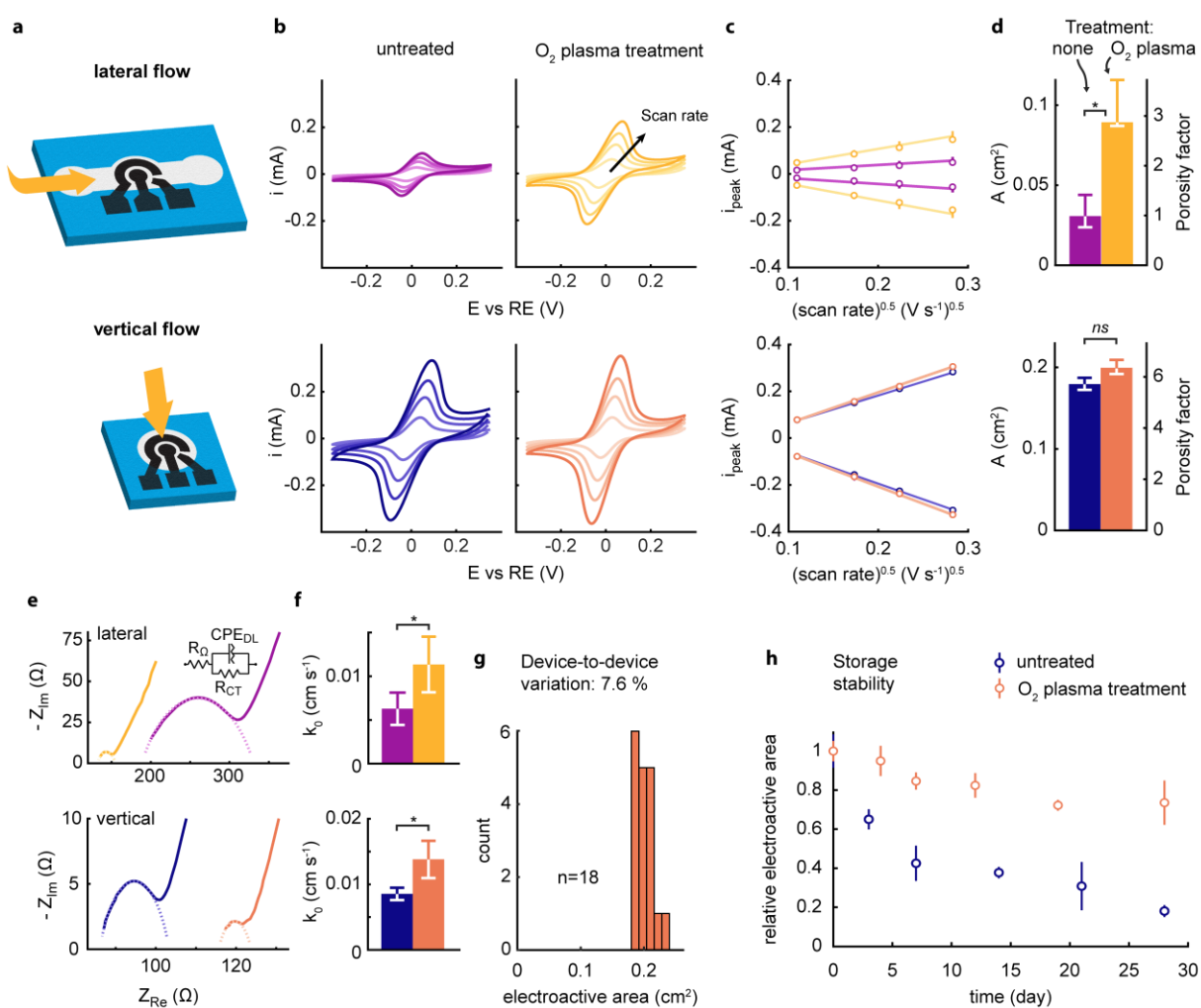


**Fig. 4. LIG-E electrochemical properties depend on electrode wicking.** (a) Electrochemical characterization of three-electrode cells made of LIG-E in lateral (top) and vertical (bottom) flow configurations. (b) Comparison of cyclic voltammetry responses for LIG-E and plasma-treated LIG-E using 10 mM  $[Fe(CN)_6]^{3-/4-}$  in 1 M KCl at scan rates of 12, 30, 50 and 80  $mV\ s^{-1}$ . (c) Randles-Ševčík plots derived from the current peak heights ( $i_{peak}$ ) with respect to scan rate, together with linear fittings. (d) Extracted electroactive areas and corresponding electrochemical porosity factors. (e) Nyquist plots revealing electrochemical impedance for LIG-E and plasma-treated LIG-E in lateral or vertical flow

configurations. Inset: the Randles circuit used to fit impedance responses (dotted lines) and extract electron transfer rates (f). (g) Statistical distribution ( $n=18$ ) of extracted electroactive area values, revealing small device-to-device variations. (h) Comparison of storage stability at room temperature and with desiccant over a period of four weeks for LIG-E and plasma-treated LIG-E.

We next evaluated the electron transfer rates of the LIG-E using impedance spectroscopy (Fig. 4e) (52). In most cases, fast electron transfer rates are desirable as they usually lead to lower Ohmic overpotentials and sharper peaks during potential sweeps. We observed that the top layer of the LIG-E, which is accessible only in the vertical flow configuration, shows a higher electron rate constant (Fig. 4f). Unexpectedly, oxygen plasma treatment also enhances the electron transfer rate. Our hypothesis is that partial etching of the LIG-E material or the presence of contaminants increases the number of exposed graphenic edges, which in turn facilitates interfacial reaction kinetics (41). Compared to other systems, the rate constant values reported here ( $k_0 \sim 0.01 \text{ cm s}^{-1}$ ) are approximately one order of magnitude higher than those fabricated by carbon screen printing and conventional laser pyrolyzation, but lower than the laser-pyrolyzed polyimide (Table S3) (21, 31, 52).

We further systematically characterized the electrochemical parameters of fabricated LIG-Es to evaluate the device-to-device variation and storage stability, which are important considerations for commercial applications and field deployability. Taking the electroactive area as the key index, our preliminary analysis indicated a device-to-device variation of less than 8% RSD (Fig. 4g) and activity loss of below 30% over four weeks of storage at ambient temperature (Fig. 4h). With the above results in mind, we concluded that the porous conductive structure of LIG-E presented here successfully translates into stable and large electroactive surfaces for electrochemical detection, with fast electron transfer rates.

### **Lateral flow injection analysis of serum samples**

Flow injection analysis (FIA) is a high-throughput analysis method in which samples are injected sequentially into a flow of carrying buffer upstream of an electrochemical detector (10). FIA paper-based devices driven by capillary flow have been reported for the analysis of small molecules in buffer or urine samples, using electrodes contacted to the paper surface (53, 54). In comparison, our LIG-E

approach offers two main advantages. First, it simplifies the device architecture by integrating the fluidic channel and electrodes together, and second, it analyses the entire cross-section of the fluid flowing through the channel and not just the fluid in contact with the top surface.

For the FIA application, we designed the device in a lateral flow configuration, which allows spatial separation of individual components, including buffer inlet, injection port, and electrodes, along the flow direction. As a clinically relevant assay, we chose to analyse alkaline phosphatase (ALP) in serum. ALP is a first-line biomarker for the diagnosis and treatment of liver, bone, and parathyroid diseases (55). Typical concentrations of serum ALP in adults range between 30 and 120 U L<sup>-1</sup> (activity unit; 1 U = 1 μmol *p*-nitrophenol per minute at 37 °C) (56). A deviation from this range represents the starting point of clinical decision algorithms for a variety of diseases, including hypophosphatasia (57).

Figures 5a and 5b present a schematic and photograph of our FIA device. A steady capillary flow is first established between the buffer reservoir and absorbent pad, laterally moving along the channel and across the embedded LIG-Es. The sample is mixed with the *p*-aminophenyl phosphate (*p*-APP) substrate, incubated, and then injected into the device upstream of the LIG-Es. We performed real-time detection via chronoamperometry (Figs. 5c and S15). Our optimized protocol allows the injection and analysis of up to 24 samples within 20 minutes, consuming less than 500 μL of carrying buffer and 5 μL of each sample (Fig. 5d). For the spiked buffer samples, the assay exhibits good linearity within the clinically relevant range, with a detection limit of 1.4 U L<sup>-1</sup> (Fig. 5e); a value comparable with the lower working range of gold-standard benchtop systems (58).

For the analysis of serum samples, we found that the effects of the complex sample matrix and increased viscosity hinder the comparison with predetermined calibration values. Accordingly, we used the standard addition method, which has been shown to effectively mitigate matrix contributions in calibration-free protocols (59). We analysed three serum samples and found alkaline phosphatase activities of 35±1, 105±6 and 8±4 U L<sup>-1</sup> (Fig. 5f and 5g). Remarkably, and despite the large surface area of LIG-E, we did not observe considerable electrode fouling in serum tests. We attribute this to the low-

volume requirements and the regeneration of electrode surface by the buffer flow. We benchmarked against the gold standard test, a plate reader monitoring absorption kinetics with *p*-nitrophenyl phosphate as a substrate (Figs. S16 and S17), and observed excellent agreement ( $33.6 \pm 0.6$ ,  $106.7 \pm 0.5$  and  $7.4 \pm 0.1$  U L<sup>-1</sup>, respectively; Fig. 5h) between the datasets.

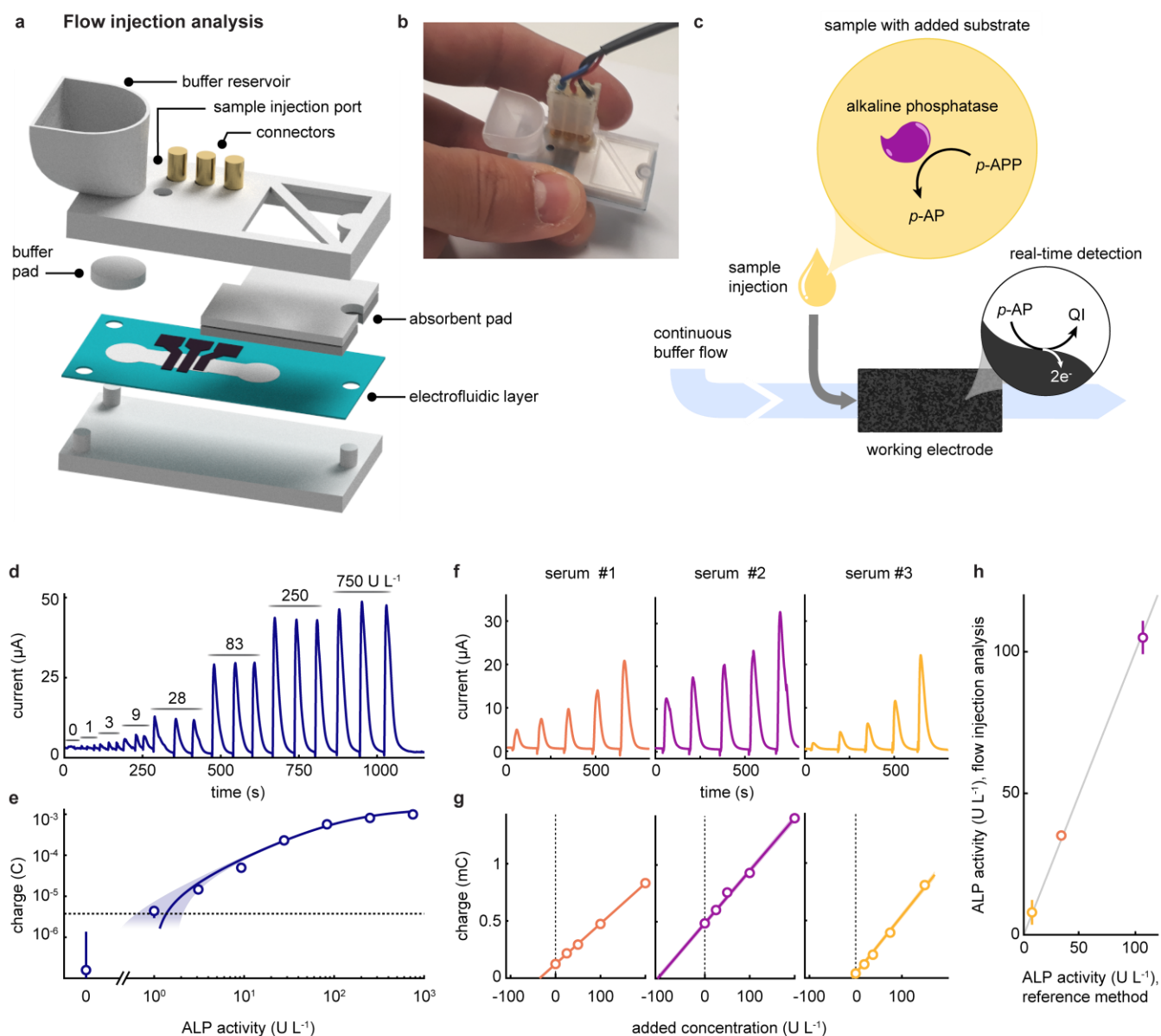


**Fig. 5. Lateral flow injection analysis of alkaline phosphatase in serum.** (a) Exploded-view schematic of the device architecture. A steady capillary flow is established between the buffer reservoir and absorbent pad, laterally moving along the channel and across the embedded LIG-Es in the electrofluidic layer. (b) Photograph of the assembled device connected to a potentiostat. (c) Schematic diagram of the ALP detection assay in serum, with real-time detection on the porous electrodes allowing injection of multiple samples in sequence. (d) Measurement of ALP activity in spiked buffer samples in a dilution series. (e) Corresponding signals from the integrated peaks with respect to the ALP activity. (f) Measurement of ALP activity in spiked buffer samples in a dilution series. (g) Corresponding signals from the integrated peaks with respect to the ALP activity. (h) Comparison of ALP activity (U L<sup>-1</sup>) between flow injection analysis and a reference method, showing a linear relationship.

The shaded line represents the mean with three standard deviations of the negative control. (f) Analysis of the ALP activity of three unknown serum samples by the standard addition method. (g) The ALP activities were extracted by linear fittings of the response signals. (h) Comparison of measured ALP activity values with those from the gold-standard colorimetric test. *p*-AP: *p*-aminophenol; QI: 4-quinoneimine.

### **A vertical flow capture assay for the detection of HPV16-activated CRISPR reporters**

Capture assays, such as pregnancy and Covid-19 antigen tests, represent the most popular current application of  $\mu$ PADs. In these assays, capillary-driven flow is harnessed to minimize the number of user operations (most notably washing steps) compared to plate-based assays, making these devices particularly suitable for decentralized testing. Recently, the introduction of CRISPR-based biosensing has expanded our collective ability to perform molecular diagnostics at the point of care (60–62). An excellent example is the DNA Endonuclease-Targeted CRISPR Trans Reporter (DETECTR) assay, which combines recombinase polymerase amplification (RPA) with CRISPR/Cas12a signal generation to detect viral genomes with exceptional sensitivity and on short timescales (60). As the field expands, the need for methods that detect CRISPR reporters using minimal instrumentation is becoming more pressing (61, 62). With this in mind, and as a proof of concept, we developed a rapid electrochemical capture assay for HPV16, a high-risk carcinogenic subtype of HPV that benefits from early detection (63). Our approach integrates the DETECTR assay with electrochemical detection of the CRISPR reporters within our low-cost platform. Due to the ‘signal-off’ nature of reporter detection (i.e. a strong positive sample leads to a low signal), electrochemical readout is highly advantageous, as it simplifies result interpretation by providing an unambiguous digital result for the untrained user.

We chose to construct the device around a vertical flow configuration (Fig 6a and 6b). Although vertical flow assays are less common than their lateral flow counterpart, they have had considerable recent commercial success due to the faster assay time resulting from enlarged flow cross sections (50). Our design sandwiches a nitrocellulose capture layer between a receiving sample pad and the LIG-E, thus avoiding tedious chemical functionalization on the electrode. The working principle relies on the capture of ssDNA reporters on the antibody-functionalized nitrocellulose pad (Fig. 6c). Specifically, in the

presence of HPV16 amplicons, reporters are cleaved and labels flow through the LIG-E without generating signal. Conversely, for a negative sample, reporters remain uncleaved, thus ensuring ample binding sites for labelling. Labelling and signal generation then take place through amplification of ALP, a standard enzymatic label for linked immunoassays (Fig. S18).

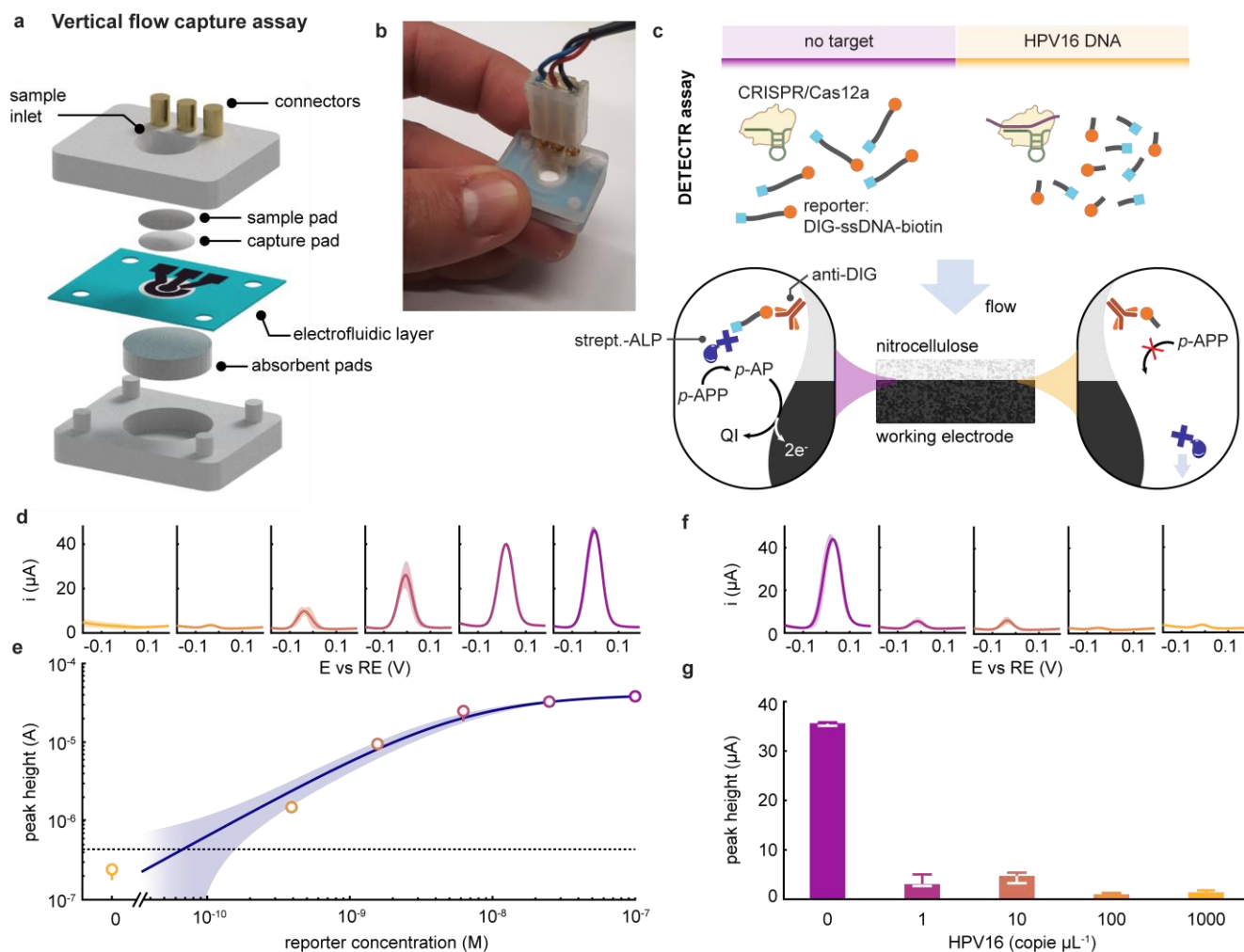


**Fig. 6. Vertical flow capture assay for electrochemical detection of HPV16.** (a) Exploded-view schematic of the vertical flow device made by layering structure of the capture pad, LIG-E, and absorbent pad. (b) Photograph of the assembled device connected to a potentiostat. (c) Schematic of the DETECTR assay with electrochemical detection of reporters captured on the porous electrode. (d) Representative square-wave voltammograms for buffer samples with increasing reporter concentrations in the vertical flow capture assay. (e) Corresponding response curve and the Langmuir fit for reporter detection. The shaded line includes three standard deviations of the negative control. (f) Square-wave voltammograms and (g) corresponding peak heights for the detection of HPV16 with the full DETECTR assay for genome concentrations of 0, 1, 10, 100 and 1000 copies  $\mu\text{L}^{-1}$ , showing strong quenching of the signal at even 1 copy  $\mu\text{L}^{-1}$  of HPV16.

We designed the device to saturate after the addition of enzymatic substrate and quantified the amount of captured label by square wave voltammetry (Figs. S19 and S20). For the direct detection of CRISPR reporter, we observe a lower detection limit of 67 pM and upper limit of quantification of 60 nM of reporter (Figs. 6d and 6e). Combined with DETECTR, we observed strong quenching of the voltammetry signal in the presence of HPV16 (Fig. 6f) and achieved a lower limit of detection of 1 copy  $\mu\text{L}^{-1}$  of HPV16, using the WHO reference standard for HPV16 (Fig. 6g and S21). Remarkably, we found that these results were comparable to benchtop fluorescence data using a plate reader (Fig. S22). This assay demonstrates the usefulness of the LIG-E platform to perform capture assays for high-performance molecular detection, without sacrificing the operational simplicity of colorimetric devices.

## Conclusions

We have presented a platform that combines paper microfluidics and laser-pyrolyzed electronics. We elucidated the formation of nanoscale graphenic domains upon laser-induced pyrolysis of cellulose and found that the LIG-E not only conserves the microscale structure and mesoporous nature of cellulose fibers, but can also retain the wetting and wicking behaviour due to the oxygen-rich surface functional groups. The process enables the independent design of capillary and electronic current pathways and overlays. The LIG-E exhibits high electrochemical porosity and electron transfer rates. We have demonstrated two clinically relevant assays using the lateral and vertical flow configurations. The former is a flow injection analysis device for alkaline phosphatase detection of serum samples, showing high throughput (> 1 assay per minute) and accurate calibration-free quantification by standard addition. The latter is a capture assay for the detection of DETECTR reporters, reaching a low HPV16 detection limit of 1 copy  $\mu\text{L}^{-1}$  with rapid electrochemical readout. We anticipate that the unique porous morphology together with the high conductivity and electroactivity of LIG-Es could open doors to new applications in the field of clinical diagnostics, environmental and food monitoring, wearable sensing, and the broader realms of material electronics.

## Material and Methods

### Fabrication of the electrofluidic layers

Cellulose paper (CF3, Cytiva) was saturated with 0.8 M (92 g/L) ammonium sulfamate ( $\text{NH}_4\text{SO}_3\text{NH}_2$ , > 98%, Sigma) using a brush and left to dry overnight. Next, the LIG-Es were fabricated using a  $\text{CO}_2$  laser engraver (100 W, Speedy 300, Trotec) equipped with a 1.5-inch focus lens and operated using the following parameters (unless indicated otherwise): power 18 (measured value: 4.8 W), speed 5 (measured value: 16 cm/s), defocus 10 mm, laser pulsing 1000 pulses per inch (PPI), line spacing 333 lines per inch (LPI). The lasing process was performed under a constant stream of nitrogen. The LIG-Es were then rinsed with deionized water, isopropanol and acetone and left to dry overnight. Optionally, the LIG-Es were treated by oxygen plasma for 90 seconds at 90 W (Atto, Diener electronic). Wax patterns were created by first printing a full layer of wax (Xerox Colorqube 8570) on a transparency (X-100, Folex), following by removal of the hydrophilic channel areas using the laser cutter (power 6, speed 1). The wax pattern was transferred onto the paper layer via lamination at a temperature of 110 °C (Photonex 325lsi, GMP). All designs (channels and electrodes) are created in Adobe Illustrator CS6.

### Structural and chemical characterization

The sheet resistance,  $R_s$ , (unit:  $\Omega \text{ sq}^{-1}$ ) was measured using the four-probe technique, with the probes configured in a square with 2 mm spacing. The sheet resistance was calculated according to,

$$R_s = \frac{2\pi}{\ln 2} \cdot \frac{E}{i}$$

where  $E$  (in V) and  $i$  (in A) are the applied voltage and measured current, respectively (64).

Raman spectroscopy was performed using a confocal Raman microscope (Renishaw InVia) using a 532 nm laser (max power 50 mW), a 20× objective (Zeiss) and a 1800 lines  $\text{mm}^{-1}$  grating. The exposure time was 3 seconds for a laser power of 5%, and spectra were recorded between 1237 and 2796  $\text{cm}^{-1}$  and averaged over 10 accumulations. Spectra were corrected for background effects by subtracting a linear function that compensates for autofluorescence of the cellulose paper. Peaks were analysed by

fitting a Lorentzian function with four components for the D-, G-, 2D- (double, 2D<sub>1</sub> & 2D<sub>2</sub>) bands respectively (35, 37), i.e.

$$f = \sum_{i=1}^4 \frac{a_i}{1 + \left(\frac{x - x_i}{c_i}\right)^2}$$

The individual integrated peak signals  $S_i$  are given by  $S_i = \pi c_i a_i$ , and used for analysis and discussion.

Wide-angle X-ray scattering (WAXS) measurements were performed using a laboratory powder X-ray diffractometer (XPert PRO, PANalytical). The X-ray tube was operated at 45 kV and 40 mA with Cu K $\alpha$  radiation (0.1542 nm). The LIG-E material was scrapped off the cellulose paper and gently placed on a zero-diffraction plate. Measurements were performed from  $2\theta = 8^\circ$  to  $2\theta = 100^\circ$  with a step size of  $0.20^\circ$ . The length of the scattering vector,  $q$ , (in nm<sup>-1</sup>) is given by  $q = 4\pi/\lambda \sin(\theta)$ , with  $2\theta$  being the scattering angle and  $\lambda$  the X-ray wavelength ( $\lambda_{\text{Cu,K}\alpha} = 0.1542$  nm). The three main peaks considered are the (002), (10) and (11) peaks. The shoulders observed on the (10) and (11) peaks are attributed to higher order planes, namely (004) and (006), respectively, and were not accounted for during the fitting process due to their minor contributions. Crystallite dimensions were calculated using the Scherrer equation, which considers the broadening of scattering peaks in reciprocal space (40). Each peak was fitted individually using a Gaussian peak function on top of a linear background, as detailed elsewhere (34, 65). The crystallites dimensions were estimated using (40):

$$L = K \frac{2\pi}{w}$$

$K$  is an application-specific coefficient and  $w$  the full width at half maximum of the scattering peak. We used  $K = 0.91$  for  $L_c$  from the (002) peak and  $K = 1.84$  for  $L_a$  from the (10) peak as defined by Warren (40). The Scherrer equation has been shown to be valid for graphitic materials with crystallite sizes above 2 nm (34, 40). The interlayer spacing was computed from the (002) peak position using Bragg's law in the reciprocal space, i.e.  $d_{002} = 2\pi/q$ .

Scanning electron microscopy (SEM) measurements were performed on a digital field emission SEM (Ultra 55, Zeiss) with an electron beam energy of 5 keV, an aperture of 30  $\mu\text{m}$ , and secondary electron detector (InLens, Zeiss). Samples were prepared by sputter coating of a PdAu alloy. The spatial elemental composition along a line was measured by energy-dispersive X-ray (EDX) spectroscopy on the same machine with an electron beam energy of 10 keV and aperture of 120  $\mu\text{m}$ .

The surface atomic composition was analysed by X-ray photoelectron spectroscopy (XPS) on a Quantera II Surface Analysis Equipment (PHI). A survey spectrum was first acquired between 0 and 1350 eV followed by high resolution acquisition for C(1s), N(1s), O(1s) and S(2p). Data were analysed using CasaXPS software.

Pore size distributions were investigated via mercury porosimetry on an automated porosimeter (Autopore IV, micromeritics) using 22  $\text{cm}^2$  of sample (0.3 g) and a penetrometer with 0.412 mL stem volume. Pore size distributions were computed assuming an Hg contact angle of  $130^\circ$ , and an Hg surface tension of 485  $\text{dynes cm}^{-1}$ . A pressure ramp from 3.3 kPa to 137 MPa was applied to the sample (pore diameter range: 9 nm to 370  $\mu\text{m}$ , i.e. meso/macro-porosity). The pore size distribution was depicted against the absorption volume (in  $\mu\text{L cm}^{-2}$ ) for each pore size.

### **Wetting properties**

Water contact angles were measured using a MCA-3 Microscopic Contact Angle Goniometer (Kyowa Interface Science). Droplets of water ( $\sim 0.5 \mu\text{L}$ ) were dispensed using a glass capillary with a 50  $\mu\text{m}$  tip diameter. Images were recorded with a calibrated side camera (640 x 480 pixels, 6.97  $\mu\text{m}/\text{pixel}$ ) at 40 frames per seconds.

Lateral flow profiles were measured using a 3D-printed set-up reported elsewhere (66), and imaged using a smartphone camera (Samsung Galaxy A3 2017) at 30 frames per second. The strips were laser cut to a size of 4 x 40 mm and mounted on an adhesive backing card (KN-2211, Kenosha) with a sample pad and absorbent pad (CF6, Cytiva). For our investigations, we included LIG-E of 4 mm length on the strip along the flow path. 200  $\mu\text{L}$  of deionized water was pipetted onto the sample pads and the flow

front monitored with a camera. The front was extracted from the video by thresholding the averaged pixel intensity values along the flow path with a MATLAB (R2022b) script.

Vertical flow profiles were measured on the contact angle setup. All layers were laser cut to a diameter of 7.5 mm and were arranged as follows in a 3D-printed holder (from top to bottom): 2 layers cellulose (CF3, Cytiva), 1 layer of cellulose with or without pyrolyzed electrode, 2 layers of cellulose, and 2 layers of absorbent pad (CF6, Cytiva). A volume of 120  $\mu\text{L}$  of contrast dye (6 mg/mL Allura Red AC in water, Sigma) was drop cast onto the stack. The profile was monitored at 50 frames per second and extracted by thresholding of the pixel intensity values.

### Electrochemical characterization

All electrochemical measurements were performed using a three-electrode configuration with a pseudo-reference (LIG-E) electrode, and no pre-treatment of the electrodes. Cyclic voltammetry experiments were performed on a potentiostat (PGSTAT204, Metrohm Autolab) using a solution of 10 mM  $[\text{Fe}(\text{CN})_6]^{3-/4-}$  (Sigma Aldrich) in 1 M KCl at scan rates of 80, 50, 30 and 12  $\text{mV s}^{-1}$  from -0.25 V to 0.25 V. The electroactive area was extracted from the slope of the peak current values,  $i_p$ , plotted against the square root of the scan rate,  $v$ , according to the Randles-Ševčík equation for a diffusion-controlled reversible system (67, 68), i.e.

$$i_p = 2.69 \cdot 10^5 n^{3/2} A D^{1/2} C v^{1/2}$$

Here  $n$  is the number of electrons transferred,  $A$  the electroactive area (in  $\text{cm}^2$ ),  $D = 0.6 \times 10^{-5} \text{ cm}^2 \text{ s}^{-1}$  the diffusion coefficient of ferro/ferricyanide (in  $\text{cm}^2 \text{ s}^{-1}$ ),  $C$  the redox probe concentration (in  $\text{mol cm}^{-3}$ ) and  $v$  the scan rate (in  $\text{V s}^{-1}$ ). The electrochemical porosity factor ( $\eta$ ) was calculated by dividing the electroactive area by the geometric (projected) area of the design. Electron transfer rates were measured by electrochemical impedance spectroscopy (EIS) on a potentiostat (Vionic, Metrohm) using the same redox probe solution as above, and with the following parameters: DC offset of 0 V versus open circuit potential, 10 mV amplitude, frequency range from 1 Hz to 200 kHz (52). A Randles circuit was fitted to the high-frequency data in the EIS Nyquist plot using the Nova 2.1 software (Metrohm Autolab). The

Randles circuit comprised a solution resistance,  $R_{\Omega}$ , followed by two components in parallel: a constant phase element for the double layer,  $CPE_{DL}$ , and the charge transfer resistance,  $R_{CT}$ . The electron transfer rate,  $k_0$ , (in  $\text{cm s}^{-1}$ ) was calculated from (51):

$$k_0 = \frac{i_0}{F A C} \quad \text{with } i_0 = \frac{R T}{F R_{ct}}$$

with  $F$ ,  $R$  and  $T$  being the Faraday constant, the gas constant and the temperature (in K), respectively. The ferro/ferricyanide concentration  $C$  and electrochemical surface area  $A$  were taken from the cyclic voltammetry measurement.

### **Flow injection analysis assay**

HOLDERS were designed in FreeCAD and 3D printed on a stereolithography 3D printer (SL1S, Prusa) with transparent resin (Clear Tough Resin, 3DM) using the manufacturer standard parameters. All shapes of paper and nitrocellulose were cut to size with the laser cutter. The design included a buffer reservoir with 1 mL capacity, which is contacted to the electrofluidic layer through a 8.3 mm diameter buffer pad (CF6, Cytiva). After flowing through the electrodes, the buffer was absorbed by two absorbent pads with 450  $\mu\text{L}$  capacity each (CF6, Cytiva). The assay was performed as follows. The sample (10  $\mu\text{L}$ ) was mixed with 10  $\mu\text{L}$  of standard. The standard comprised alkaline phosphatase (P7923, Sigma) with a pre-calibrated activity. Next, 2  $\mu\text{L}$  of 100 mM *p*-aminophenyl phosphate ( $\geq 97\%$ , Adipogen) in 1 M Tris-HCl pH 9.8 with 200 mM  $\text{MgCl}_2$  were added to the mixture followed by incubation for 20 minutes at 37  $^{\circ}\text{C}$ . The samples were put on ice before injection (5  $\mu\text{L}$  injection volume) into the device. The following sera were analyzed: calf serum C8056 (Sigma), human serum H4522 (Sigma) and goat serum G9023 (Sigma). All sera samples were centrifuged at 2 krcf for 10 minutes before use. The electrochemical measurements were performed in chronoamperometry mode (PGSTAT 204, Metrohm) with an applied voltage of 0.25 V vs RE, and sampling resolution of 10 ms. The signals were computed by integrating the current peaks with subtraction of a linear background.

For comparison, the alkaline phosphatase activities were evaluated on a plate reader using the standard colorimetric assay (58). In short, 100  $\mu\text{L}$  of sample was prepared containing the reference standard or serum at five-fold dilution in 100 mM Tris-HCl pH 9.8 and 20 mM  $\text{MgCl}_2$ . Then 10  $\mu\text{L}$  of 100 mM *p*-nitrophenyl phosphate (>99%, Roth AG) was spiked into the sample in a 96-well plate and incubated at 37 °C. Absorption was monitored at 405 nm and the activity (in IU, defined as 1 IU = 1  $\mu\text{mol}$  *p*-nitrophenol per min) calculated via the kinetics method from the slope of the absorption values. For calibration of the absorption readout, a standard curve was measured using calibration solutions of 10 mM *p*-nitrophenol (N7660, Sigma) at equivalent volumes.

### **DETECTR capture assay**

The vertical flow capture device comprised (from top to bottom) a sample pad (CF1, Cytiva, 8 mm diameter), a capture nitrocellulose layer (AE98, Cytiva, 8 mm diameter), the electrofluidic layer and two absorbent pads with 275  $\mu\text{L}$  capacity (CF6, Cytiva, 11.3 mm diameter). The nitrocellulose layer was functionalized with anti-digoxigenin antibodies by drop casting 3  $\mu\text{L}$  anti-DIG goat IgG (MB-7000, Vector Laboratories) at 1 mg  $\text{mL}^{-1}$  on the membrane and left to dry overnight. For the target, the 1st International Standard for Human Papillomavirus (HPV) Type 16 DNA was used (ref 06/202, GenBank sequence K02718, National Institute for Biological Standards and Control). The full length of the genome was amplified by PCR using the Q5® High-Fidelity 2X Master Mix (New England Biolabs) with no deviations from the manufacturer instructions (98 °C, 30 s > 35 cycles [98 °C, 10 s > 71 °C, 30s > 72 °C, 320 s] > 72 °C, 2 min) and with the following primers. Forward: GCTTCGCTACTTGGAGCCACT, Reverse: GATATAGGCGCCAGCAACCGCA. Amplicons were purified using the NucleoSpin® Gel and PCR Clean-up kit (Macherey-Nagel) according to the user manual, and analysed by gel electrophoresis (1% agarose gel).

The DETECTR assay combines recombinase polymerase reaction (RPA) with CRISPR-based detection, and followed closely the work of Chen *et al.* (60). First, the HPV16-targeting CRISPR complex was prepared by incubating a mixture of 15.75  $\mu\text{L}$  nuclease-free water, 2  $\mu\text{L}$  10X NEBuffer 2.1 (New England Biolabs), 1  $\mu\text{L}$  LbCas12a 1  $\mu\text{M}$  (New England Biolabs) and 1.25  $\mu\text{L}$  of guide RNA 1  $\mu\text{M}$

(HPV16-specific sequence targeting the L1 gene: UAAUUUCUACUAAGUGUAGAUUGAAGUAGAU AUGGCAGCAC) for 90 min at 37 °C. The RPA reaction followed the TwistAmp® Basic Kit (TwistDx) manual. In brief, a mixture containing 29.5 µL rehydration buffer, 13.2 µL target, and 2 × 2.4 µL of each primer was added to the lyophilized RPA reagents. The reaction was started with the injection of 2.5 µL MgOAc 280 mM and incubated at 39 °C for 25 min. RPA primers targeting the HPV16 L1-gene: forward TTGTTGGGGTAACCAACTATTTGTTACTGTT, reverse CCTCCCCATGTCGTAGGTACTCCTTAAAG. Then, 2 µL of RPA mixture was spiked into a solution of 80 µL NEBuffer 2.1 (New England Biolab), 18 µL of the prepared CRISPR complex and 1 µL of reporter oligo 10 µM (biotin-5'-TTATTATT-3'-digoxigenin, Microsynth AG), and incubated for 90 minutes.

Electrochemical detection of the reporters was performed on the vertical flow capture device. The following solutions were freshly prepared. Blocking buffer 5X: 5 wt% bovine serum albumin (> 96%, A4503, Sigma), 50 mM Tris·HCl pH 7.5, 0.5 vol% Tween 20; Label solution: streptavidin-alkaline phosphatase conjugate (1 mg mL, S2890, Sigma) 200-fold diluted in Blocking buffer 5X. Rinsing buffer: 10 mM Tris·HCl pH 7.5, 0.5 vol% Tween 20. Substrate solution: 9 mM *p*-aminophenyl phosphate in 100 mM Tris·HCl pH 10, 20 mM MgCl<sub>2</sub>. The sample constituted 10 µL DETECTR assay solution with 30 µL deionized water and 10 µL of Label solution. The device was first rinsed with 50 µL of Blocking buffer 1X, followed by the injection of 50 µL of sample, 130 µL of rinsing buffer and 120 µL Substrate solution. After 15 minutes at room temperature, a square wave voltammogram was acquired between -0.2 and 0.25 V with 5 mV step, 25 mV pulse amplitude and 2.5 Hz pulse frequency.

### **Statistical analysis**

Unless mentioned otherwise, measurements are performed in triplicate and the median value shown. The error bars correspond to the associated 25-75% percentile range. In the main body of the text, values are referred to their median and the largest difference to either quartile indicated. Significance and *p*-

values are computed using a two-sample Kolmogorov-Smirnov test. In the case of fitted curves, the confidence interval is shown as a shaded area for one standard deviation in each direction.

## References

1. D. Zhao, Y. Zhu, W. Cheng, W. Chen, Y. Wu, H. Yu, Cellulose-Based Flexible Functional Materials for Emerging Intelligent Electronics. *Adv. Mater.* **33**, 2000619 (2021).
2. N. K. Khosla, J. M. Lesinski, M. Colombo, L. Bezinge, A. J. deMello, D. A. Richards, Simplifying the complex: accessible microfluidic solutions for contemporary processes within in vitro diagnostics. *Lab Chip.* **22**, 3340–3360 (2022).
3. E. Noviana, C. P. McCord, K. M. Clark, I. Jang, C. S. Henry, Electrochemical paper-based devices: Sensing approaches and progress toward practical applications. *Lab Chip.* **20**, 9–34 (2020).
4. D. Najjar, J. Rainbow, S. Sharma Timilsina, P. Jolly, H. de Puig, M. Yafia, N. Durr, H. Sallum, G. Alter, J. Z. Li, X. G. Yu, D. R. Walt, J. A. Paradiso, P. Estrela, J. J. Collins, D. E. Ingber, A lab-on-a-chip for the concurrent electrochemical detection of SARS-CoV-2 RNA and anti-SARS-CoV-2 antibodies in saliva and plasma. *Nat. Biomed. Eng.* **6**, 968–978 (2022).
5. S. Olenik, H. S. Lee, F. Güder, The future of near-field communication-based wireless sensing. *Nat. Rev. Mater.* **6**, 286–288 (2021).
6. P. Teengam, W. Siangproh, S. Tontisirin, A. Jiraseree-amornkun, N. Chuaypen, P. Tangkijvanich, C. S. Henry, N. Ngamrojanavanich, O. Chailapakul, NFC-enabling smartphone-based portable amperometric immunosensor for hepatitis B virus detection. *Sensors Actuators, B Chem.* **326**, 128825 (2021).
7. W. Dungchai, O. Chailapakul, C. S. Henry, Electrochemical detection for paper-based microfluidics. *Anal. Chem.* **81**, 5821–5826 (2009).
8. K. Abe, K. Kotera, K. Suzuki, D. Citterio, Inkjet-printed paperfluidic immuno-chemical sensing device. *Anal. Bioanal. Chem.* **398**, 885–893 (2010).
9. N. X. Williams, G. Bullard, N. Brooke, M. J. Therien, A. D. Franklin, Printable and recyclable carbon electronics using crystalline nanocellulose dielectrics. *Nat. Electron.* **2021 44**, **4**, 261–268 (2021).
10. N. F. Barros Azeredo, M. S. Ferreira Santos, J. R. Sempionatto, J. Wang, L. Angnes, Screen-Printed Technologies Combined with Flow Analysis Techniques: Moving from Benchtop to Everywhere. *Anal. Chem.* **94**, 250–268 (2022).
11. S. Cinti, D. Moscone, F. Arduini, Preparation of paper-based devices for reagentless electrochemical (bio)sensor strips. *Nat. Protoc.* **14**, 2437–2451 (2019).
12. D. Maier, E. Laubender, A. Basavanna, S. Schumann, F. Güder, G. A. Urban, C. Dincer, Toward Continuous Monitoring of Breath Biochemistry: A Paper-Based Wearable Sensor for Real-Time Hydrogen Peroxide Measurement in Simulated Breath. *ACS Sensors.* **4**, 2945–2951 (2019).
13. C. T. Kokkinos, D. L. Giokas, A. S. Economou, P. S. Petrou, S. E. Kakabakos, Paper-Based Microfluidic Device with Integrated Sputtered Electrodes for Stripping Voltammetric Determination of DNA via Quantum Dot Labeling. *Anal. Chem.* **90**, 1092–1097 (2018).
14. K. J. Klunder, Z. Nilsson, J. B. Sambur, C. S. Henry, Patternable Solvent-Processed

- Thermoplastic Graphite Electrodes. *J. Am. Chem. Soc.* **139**, 12623–12631 (2017).
15. E. Noviana, K. J. Klunder, R. B. Channon, C. S. Henry, Thermoplastic Electrode Arrays in Electrochemical Paper-Based Analytical Devices. *Anal. Chem.* **91**, 2431–2438 (2019).
  16. Y. Xu, G. Zhao, L. Zhu, Q. Fei, Z. Zhang, Z. Chen, F. An, Y. Chen, Y. Ling, P. Guo, S. Ding, G. Huang, P. Y. Chen, Q. Cao, Z. Yan, Q. Fe, Z. Zhang, Z. Chen, F. An, Y. Chen, Y. Ling, P. Guo, S. Ding, G. Huang, P. Y. Chen, Q. Cao, Z. Yan, Pencil-paper on-skin electronics. *Proc. Natl. Acad. Sci. U. S. A.* **117**, 18292–18301 (2020).
  17. M. M. Hamed, A. Ainla, F. Güder, D. C. Christodouleas, M. T. Fernández-Abedul, G. M. Whitesides, Integrating Electronics and Microfluidics on Paper. *Adv. Mater.* **28**, 5054–5063 (2016).
  18. J. Lin, Z. Peng, Y. Liu, F. Ruiz-Zepeda, R. Ye, E. L. G. Samuel, M. J. Yacaman, B. I. Yakobson, J. M. Tour, Laser-induced porous graphene films from commercial polymers. *Nat. Commun.* **5**, 1–8 (2014).
  19. Y. Chyan, R. Ye, Y. Li, S. P. Singh, C. J. Arnusch, J. M. Tour, Laser-Induced Graphene by Multiple Lasing: Toward Electronics on Cloth, Paper, and Food. *ACS Nano*. **12**, 2176–2183 (2018).
  20. E. R. Mamleyev, S. Heissler, A. Nefedov, P. G. Weidler, N. Nordin, V. V. Kudryashov, K. Länge, N. MacKinnon, S. Sharma, Laser-induced hierarchical carbon patterns on polyimide substrates for flexible urea sensors. *npj Flex. Electron.* **3**, 2 (2019).
  21. P. Nayak, N. Kurra, C. Xia, H. N. Alshareef, Highly Efficient Laser Scribed Graphene Electrodes for On-Chip Electrochemical Sensing Applications. *Adv. Electron. Mater.* **2**, 1600185 (2016).
  22. R. R. A. Soares, R. G. Hjort, C. C. Pola, K. Parate, E. L. Reis, N. F. F. Soares, E. S. Mclamore, J. C. Claussen, C. L. Gomes, Laser-Induced Graphene Electrochemical Immunosensors for Rapid and Label-Free Monitoring of Salmonella enterica in Chicken Broth. *ACS Sensors*. **5**, 1900–1911 (2020).
  23. Z. Wan, M. Umer, M. Lobino, D. Thiel, N. T. Nguyen, A. Trinchi, M. J. A. Shiddiky, Y. Gao, Q. Li, Laser induced self-N-doped porous graphene as an electrochemical biosensor for femtomolar miRNA detection. *Carbon*. **163**, 385–394 (2020).
  24. F. Gerstl, U. Pongkitdachoti, F. Unob, A. J. Baeumner, Miniaturized sensor for electroanalytical and electrochemiluminescent detection of pathogens enabled through laser-induced graphene electrodes embedded in microfluidic channels. *Lab Chip*. **22**, 3721–3733 (2022).
  25. Y. Chyan, J. Cohen, W. Wang, C. Zhang, J. M. Tour, Graphene Art. *ACS Appl. Nano Mater.* **2**, 3007–3011 (2019).
  26. H. Park, M. Kim, B. G. Kim, Y. H. Kim, Electronic Functionality Encoded Laser-Induced Graphene for Paper Electronics. *ACS Appl. Nano Mater.* **3**, 6899–6904 (2020).
  27. B. Kulyk, B. F. R. Silva, A. F. Carvalho, S. Silvestre, A. J. S. Fernandes, R. Martins, E. Fortunato, F. M. Costa, Laser-Induced Graphene from Paper for Mechanical Sensing. *ACS Appl. Mater. Interfaces*. **13**, 10210–10221 (2021).

28. B. Kulyk, B. F. R. Silva, A. F. Carvalho, P. Barbosa, A. V. Girão, J. Deuermeier, A. J. S. Fernandes, F. M. L. Figueiredo, E. Fortunato, F. M. Costa, Laser-Induced Graphene from Paper by Ultraviolet Irradiation: Humidity and Temperature Sensors. *Adv. Mater. Technol.* **7**, 2101311 (2022).
29. W. R. de Araujo, C. M. R. Frasson, W. A. Ameku, J. R. Silva, L. Angnes, T. R. L. C. Paixão, Single-Step Reagentless Laser Scribing Fabrication of Electrochemical Paper-Based Analytical Devices. *Angew. Chemie - Int. Ed.* **56**, 15113–15117 (2017).
30. A. Bezerra Martins, A. Lobato, N. Tasić, F. J. Perez-Sanz, P. Vidinha, T. R. L. C. Paixão, L. Moreira Gonçalves, Laser-pyrolyzed electrochemical paper-based analytical sensor for sulphite analysis. *Electrochem. commun.* **107**, 106541 (2019).
31. T. Pinheiro, S. Silvestre, J. Coelho, A. C. Marques, R. Martins, M. G. F. Sales, E. Fortunato, Laser-Induced Graphene on Paper toward Efficient Fabrication of Flexible, Planar Electrodes for Electrochemical Sensing. *Adv. Mater. Interfaces.* **8**, 2101502 (2021).
32. P. Gao, T. Kasama, J. Shin, Y. Huang, R. Miyake, A Mediated Enzymatic Electrochemical Sensor Using Paper-Based Laser-Induced Graphene. *Biosensors.* **12**, 995 (2022).
33. T. S. D. Le, H. P. Phan, S. Kwon, S. Park, Y. Jung, J. Min, B. J. Chun, H. Yoon, S. H. Ko, S. W. Kim, Y. J. Kim, Recent Advances in Laser-Induced Graphene: Mechanism, Fabrication, Properties, and Applications in Flexible Electronics. *Adv. Funct. Mater.* **32**, 2205158 (2022).
34. G. A. Zickler, B. Smarsly, N. Gierlinger, H. Peterlik, O. Paris, A reconsideration of the relationship between the crystallite size  $L_a$  of carbons determined by X-ray diffraction and Raman spectroscopy. *Carbon.* **44**, 3239–3246 (2006).
35. D. B. Schuepfer, F. Badaczewski, J. M. Guerra-Castro, D. M. Hofmann, C. Heiliger, B. Smarsly, P. J. Klar, Assessing the structural properties of graphitic and non-graphitic carbons by Raman spectroscopy. *Carbon.* **161**, 359–372 (2020).
36. D. B. Schüpfer, F. Badaczewski, J. Peilstöcker, J. M. Guerra-Castro, H. Shim, S. Firoozabadi, A. Beyer, K. Volz, V. Presser, C. Heiliger, B. Smarsly, P. J. Klar, Monitoring the thermally induced transition from  $sp^3$ -hybridized into  $sp^2$ -hybridized carbons. *Carbon.* **172**, 214–227 (2021).
37. L. G. Cançado, K. Takai, T. Enoki, M. Endo, Y. A. Kim, H. Mizusaki, A. Jorio, L. N. Coelho, R. Magalhães-Paniago, M. A. Pimenta, General equation for the determination of the crystallite size  $l_a$  of nanographite by Raman spectroscopy. *Appl. Phys. Lett.* **88**, 163106 (2006).
38. A. C. Ferrari, D. M. Basko, Raman spectroscopy as a versatile tool for studying the properties of graphene. *Nat. Nanotechnol.* **8**, 235–246 (2013).
39. R. Kumar Biswas, R. K. Vijayaraghavan, P. McNally, G. M. O'Connor, P. Scully, Graphene Growth Kinetics for CO<sub>2</sub> Laser Carbonization of Polyimide. *Mater. Lett.*, 131097 (2021).
40. B. E. Warren, X-Ray Diffraction in Random Layer Lattices. *Phys. Rev.* **59**, 693 (1941).
41. M. Velický, P. S. Toth, C. R. Woods, K. S. Novoselov, R. A. W. Dryfe, Electrochemistry of the Basal Plane versus Edge Plane of Graphite Revisited. *J. Phys. Chem. C.* **123**, 11677–11685 (2019).

42. Y. Li, D. X. Luong, J. Zhang, Y. R. Tarkunde, C. Kittrell, F. Sargunraj, Y. Ji, C. J. Arnusch, J. M. Tour, Laser-Induced Graphene in Controlled Atmospheres: From Superhydrophilic to Superhydrophobic Surfaces. *Adv. Mater.* **29**, 1700496 (2017).
43. J. Liu, H. Liu, N. Lin, Y. Xie, S. Bai, Z. Lin, L. Lu, Y. Tang, Facile fabrication of superhydrophilic porous graphene with ultra-fast spreading feature and capillary effect by direct laser writing. *Mater. Chem. Phys.* **251**, 123083 (2020).
44. Y. Wang, G. Wang, M. He, F. Liu, M. Han, T. Tang, S. Luo, Multifunctional Laser-Induced Graphene Papers with Combined Defocusing and Grafting Processes for Patternable and Continuously Tunable Wettability from Superlyophilicity to Superlyophobicity. *Small.* **17**, 2103322 (2021).
45. D. Lee, T. Ozkaya-Ahmadov, C. H. Chu, M. Boya, R. Liu, A. Fatih Sarioglu, Capillary flow control in lateral flow assays via delaminating timers. *Sci. Adv.* **7**, eabf9833 (2021).
46. J. F. Evans, T. Kuwana, Radiofrequency Oxygen Plasma Treatment of Pyrolytic Graphite Electrode Surfaces. *Anal. Chem.* **49**, 1632–1635 (1977).
47. E. W. Washburn, The dynamics of capillary flow. *Phys. Rev.* **17**, 273–283 (1921).
48. R. L. Peek, D. A. Mclean, Capillary Penetration of Fibrous Materials. *Ind. Eng. Chem. - Anal. Ed.* **6**, 85–90 (1934).
49. P. Kauffman, E. Fu, B. Lutz, P. Yager, Visualization and measurement of flow in two-dimensional paper networks. *Lab Chip.* **10**, 2614–2617 (2010).
50. N. Jiang, R. Ahmed, M. Damayantharan, B. Ünal, H. Butt, A. K. Yetisen, Lateral and Vertical Flow Assays for Point-of-Care Diagnostics. *Adv. Healthc. Mater.* **8**, 1900244 (2019).
51. A. J. Bard, L. R. Faulkner, *Electrochemical methods : fundamentals and applications* (Wiley, 2001; <https://www.wiley.com/en-us/Electrochemical+Methods%3A+Fundamentals+and+Applications%2C+2nd+Edition-p-9780471043720>).
52. E. P. Randviir, A cross examination of electron transfer rate constants for carbon screen-printed electrodes using Electrochemical Impedance Spectroscopy and cyclic voltammetry. *Electrochim. Acta.* **286**, 179–186 (2018).
53. L. A. Pradela-Filho, E. Noviana, D. A. G. Araújo, R. M. Takeuchi, A. L. Santos, C. S. Henry, Rapid Analysis in Continuous-Flow Electrochemical Paper-Based Analytical Devices. *ACS Sensors.* **5**, 274–281 (2020).
54. J. Lankelma, Z. Nie, E. Carrilho, G. M. Whitesides, Paper-based analytical device for electrochemical flow-injection analysis of glucose in urine. *Anal. Chem.* **84**, 4147–4152 (2012).
55. World Health Organization, "The selection and use of essential in vitro diagnostics: report of the third meeting of the WHO Strategic Advisory Group of Experts on In Vitro Diagnostics, 2020 (including the third WHO model list of essential in vitro diagnostics)" in *WHO Technical Report Series* (Geneva, 2021), vol. 1031.
56. A. Kratz, M. Ferraro, P. M. Sluss, K. B. Lewandrowski, Normal Reference Laboratory Values. *N. Engl. J. Med.* **351**, 1548–1563 (2004).

57. N. Rifai, A. R. Horvath, C. . Wittwer, N. W. Tietz, *Tietz Textbook of Clinical Chemistry and Molecular Diagnostics* (Elsevier, St. Louis, Missouri, 6th editio., 2018; <https://books.google.ch/books?id=BBLRUI4aHhkC>).
  58. A. Killeen, J. Peters, “Laboratory Procedure Manual Alkaline Phosphatase (ALP) Roche Cobas 6000 (c501 module)” (2018), (available at <https://wwwn.cdc.gov/nchs/data/nhanes/2017-2018/labmethods/BIOPRO-J-MET-ALP-508.pdf>).
  59. S. L. R. Ellison, M. Thompson, Standard additions: myth and reality. *Analyst*. **133**, 992–997 (2008).
  60. J. S. Chen, E. Ma, L. B. Harrington, M. Da Costa, X. Tian, J. M. Palefsky, J. A. Doudna, CRISPR-Cas12a target binding unleashes indiscriminate single-stranded DNase activity. *Science*. **360**, 436–439 (2018).
  61. Z. Huang, C. J. Lyon, T. Y. Hu, CRISPR-based assays for low-resource settings. *Nat. Rev. Bioeng.* **2023**, 1–2 (2023).
  62. J. P. Broughton, X. Deng, G. Yu, C. L. Fasching, V. Servellita, J. Singh, X. Miao, J. A. Streithorst, A. Granados, A. Sotomayor-Gonzalez, K. Zorn, A. Gopez, E. Hsu, W. Gu, S. Miller, C. Y. Pan, H. Guevara, D. A. Wadford, J. S. Chen, C. Y. Chiu, CRISPR–Cas12-based detection of SARS-CoV-2. *Nat. Biotechnol.* **2020 387**. **38**, 870–874 (2020).
  63. C. B. J. Woodman, S. I. Collins, L. S. Young, The natural history of cervical HPV infection: unresolved issues. *Nat. Rev. Cancer* **2007 71**. **7**, 11–22 (2007).
  64. I. Miccoli, F. Edler, H. Pfnür, C. Tegenkamp, The 100th anniversary of the four-point probe technique: The role of probe geometries in isotropic and anisotropic systems. *J. Phys. Condens. Matter*. **27**, 223201 (2015).
  65. O. Paris, C. Zollfrank, G. A. Zickler, Decomposition and carbonisation of wood biopolymers - A microstructural study of softwood pyrolysis. *Carbon*. **43**, 53–66 (2005).
  66. M. Colombo, L. Bezinge, A. R. Tapia, C.-J. Shih, A. J. DeMello, D. A. Richards, Real-time, smartphone-based processing of lateral flow assays for early failure detection and rapid testing workflows. *Sensors & Diagnostics*. **2**, 100–110 (2023).
  67. A. Ševčík, Oscillographic polarography with periodical triangular voltage. *Collect. Czechoslov. Chem. Commun.* **13**, 349–377 (1948).
  68. J. E. B. Randles, A cathode ray polarograph. Part II. - The current-voltage curves. *Trans. Faraday Soc.* **44**, 327–338 (1948).
-

## **Acknowledgement**

We thank Erdem Siringil and the MSRL lab for granting us access to their workshop and laser cutter, Andrea Arcifa for the XPS measurements, Vera Giulimondi for mercury porosimetry, Joakim Reuteler from ScopeM for assistance with broad ion beam milling as well as Andres Rocha Tapia and Yukina Partington for gel electrophoresis. The authors are grateful to Tobias Keplinger and Christopher Dreimol for their help with Raman measurements and for the interesting discussions. D.A.R. acknowledges funding from the European Union's Horizon 2020 research and innovation programme under the Marie Skłodowska-Curie grant agreement 840232. C.J.S. is grateful for the financial support from the Swiss National Science Foundation (project number: 200021-178944).

### **Author contributions**

Conceptualization: LB, ASN, DAR, AJdM, CJS; Investigation: LB, JL; Formal analysis: LB; Writing (original draft): LB, DAR, AJdM, CJS; Writing (review and editing): LB, JL, ASN, DAR, AJdM, CJS; Visualization: LB; Supervision: LB, DAR, AJdM, CJS; Resources: DAR, AJdM, CJS; Funding acquisition: AJdM, CJS.

### **Competing interests**

L.B., A.S.-N., D.A.R., A.J.D. and C.-J.S. are inventors on a patent application related to this work (application no. EP22186139 filed on 25 July 2022 by ETH Transfer).

### **Data and materials availability**

All data are available in the main text or the supplementary materials. Designs for digital fabrication are available at: <http://dx.doi.org/10.17632/zv9x5przjh.1>.